Available online at www.sciencedirect.com
SCIENCE DIRECT®
Journal of Computational Physics 210 (2005) 401–420
JOURNAL OF COMPUTATIONAL PHYSICS
www.elsevier.com/locate/jcp

# A numerical scheme for ionizing shock waves

Necdet Aslan [a,*], Michael Mond [b]

[a] *Yeditepe University, Physics Department, Kayışdağı, 34755 İstanbul, Turkey*
[b] *Ben Gurion University, Mechanical Engineering Department, Beer Sheva, Israel*

Received 26 May 2004; received in revised form 4 January 2005; accepted 20 April 2005
Available online 21 June 2005

**Abstract**

A two-dimensional (2D) visual computer code to solve the steady state (SS) or transient shock problems including partially ionizing plasma is presented. Since the flows considered are hypersonic and the resulting temperatures are high, the plasma is partially ionized. Hence the plasma constituents are electrons, ions and neutral atoms. It is assumed that all the above species are in thermal equilibrium, namely, that they all have the same temperature. The ionization degree is calculated from Saha equation as a function of electron density and pressure by means of a nonlinear Newton type root finding algorithms. The code utilizes a wave model and numerical fluctuation distribution (FD) scheme that runs on structured or unstructured triangular meshes. This scheme is based on evaluating the mesh averaged fluctuations arising from a number of waves and distributing them to the nodes of these meshes in an upwind manner. The physical properties (directions, strengths, etc.) of these wave patterns are obtained by a new wave model: ION-A developed from the eigen-system of the flux Jacobian matrices. Since the equation of state (EOS) which is used to close up the conservation laws includes electronic effects, it is a nonlinear function and it must be inverted by iterations to determine the ionization degree as a function of density and temperature. For the time advancement, the scheme utilizes a multistage Runge–Kutta (RK) algorithm with time steps carefully evaluated from the maximum possible propagation speed in the solution domain. The code runs interactively with the user and allows to create different meshes to use different initial and boundary conditions and to see changes of desired physical quantities in the form of color and vector graphics. The details of the visual properties of the code has been published before (see [N. Aslan, A visual fluctuation splitting scheme for magneto-hydrodynamics with a new sonic fix and Euler limit, J. Comput. Phys. 197 (2004) 1–27]). The two-dimensional nature of ION-A was presented by a planar shock wave propagating over a circular obstacle. It was demonstrated that including the effects of ionization in calculating complex flows is important, even when they appear initially negligible. This code can be used to accurately simulate the nonlinear time dependent evolution of neutral or ionized plasma flows from supersonic to hypersonic regimes.


* Corresponding author.
*E-mail address:* naslan@yeditepe.edu.tr (N. Aslan).

0021-9991/$ - see front matter © 2005 Elsevier Inc. All rights reserved.
doi:10.1016/j.jcp.2005.04.018

## 1. Conservation laws for partially ionized plasma in thermal equilibrium

In this work, a partially ionized mono-atomic argon gas ($R = 287$ J/kg K) is considered. It is assumed that the electrons and the heavy particles (i.e., the atoms and the ions) are in thermal equilibrium so that all species share the same temperature, $T$. This assumption is valid for processes whose characteristic time-scales are much larger than the characteristic time for energy transfer from the heavy particles to the electrons, $\nu_\epsilon^{-1}$. Furthermore, as in argon under the conditions investigated here, the characteristic time for ionization by electron impact is equal or bigger than $\nu_\epsilon^{-1}$ (see [2]). In this case, ionization equilibrium is assumed to be maintained and hence the ionization degree, $\alpha$, may be calculated for each given density and temperature (Saha equation) at each time. Thus, it is possible to consider the electrons and the heavy particles as a single effective fluid with a single mass density and a single temperature. The equations that govern the dynamic evolution of that single fluid including electronic effects are

$$\frac{\partial \rho}{\partial t} + \nabla \cdot [\rho \mathbf{V}] = 0, \tag{1-a}$$

$$\frac{\partial \rho \mathbf{V}}{\partial t} + \nabla \cdot [\rho \mathbf{V}\mathbf{V} + (P + P_e)\tilde{I}] = 0, \tag{1-b}$$

$$\frac{\partial E}{\partial t} + \nabla \cdot [(E + P + P_e)\mathbf{V}] = 0, \tag{1-c}$$

where $\tilde{I}$ is the $3 \times 3$ unit matrix, $\rho$ is the density of heavy particles, and $P = \rho RT$ is their pressure, $P_e = \alpha P$ is the electronic pressure, $E = 1/2\rho V^2 + (P + P_e)/(\gamma - 1) + \rho\alpha R\Theta'_{\text{ion}}$ is the total energy (with $\gamma = 5/3$ and $\Theta'_{\text{ion}} = \epsilon/k = 183{,}100$ K for Ar) and $\alpha = n_e/(n_n + n_e)$ is the ionization degree which is found from Saha equation (see [3]):

$$\frac{\alpha^2}{\alpha - 1} = Z, \quad Z = b_0 \frac{T^{3/2}}{\rho} \exp\left[-\frac{\Theta'_{\text{ion}}}{T_e}\right], \quad b_0 = g m_H \left[\frac{2\pi m_e k}{h^2}\right]^{3/2}, \tag{2}$$

where $Z$ is called, here, the ionization parameter, $\epsilon$ is the ionization energy, $m_e$ is the mass of electrons, $k$ is the Boltzmann constant, $h$ is the Planck constant, and $g$ is the twice the ion to electron ratio of the statistical sums. Even though $g$ depends on the temperature, it has been shown by Mond et al. [8] that $g = 11$ yields correct results with high accuracy for the range of temperatures of interest (e.g., the temperatures <10,000 K).

### 1.1. Dimensionless forms

In order to get the dimensionless form of these conservation equations, the following parameters are introduced:

$$x' = \frac{x}{x_0}, \quad t' = \frac{t}{t_0}, \quad \rho' = \frac{\rho}{\rho_0}, \quad V' = \frac{V}{V_0}, \quad P' = \frac{P}{P_0}, \quad P'_e = \frac{P_e}{P_0}, \quad E' = \frac{E}{E_0}. \tag{3}$$

By inserting the primed (dimensionless) quantities into Eqs. (1), dimensionless forms are obtained with the following relationships between the normalizing parameters:

$$V_0 = \frac{x_0}{t_0}, \quad E_0 = P_0 = \rho_0 V_0^2 = \rho_0 R T_0. \tag{4}$$

Since ionizing shocks are considered in this work, it is convenient to normalize the equations by the pre-shock values: $T_0$, $P_0$ and $\rho_0 = P_0 R T_0$ whose values will be given later. In that case, the dimensionless pressures and energy become (by omitting primes)

$$P = \rho T, \quad P_e = \rho\alpha T, \quad E = \frac{1}{2}\rho V^2 + \frac{P + P_e}{\gamma - 1} + \rho\alpha\Theta_{\text{ion}} \tag{5}$$

with $\Theta_{\text{ion}} = 610.33$ and Saha equation turns into

$$\alpha = \frac{1}{2}\left[-Z + \sqrt{Z^2 + 4Z}\right], \tag{6}$$

where

$$Z = 857.6\frac{P^{3/2}}{\rho^{5/2}}\exp\left[-\frac{\rho\Theta_{\text{ion}}}{P}\right]. \tag{7}$$

The dimensionless form of Eqs. (1) is given in 2D as

$$\frac{\partial \mathbf{U}}{\partial t} + \frac{\partial \mathbf{F}}{\partial x} + \frac{\partial \mathbf{G}}{\partial y} = 0, \tag{8}$$

where $\mathbf{U} = [\rho, \rho V_x, \rho V_y, E]^{\mathrm{T}}$ is the conservative state vector, and $\mathbf{F}$ and $\mathbf{G}$ are the $x$ and $y$ components of the fluxes respectively. This set of equations can be written in detail as follows:

$$\frac{\partial}{\partial t}\begin{bmatrix}\rho \\ \rho V_x \\ \rho V_y \\ E\end{bmatrix} + \frac{\partial}{\partial x}\begin{bmatrix}\rho V_x \\ \rho V_x V_x + P + P_e \\ \rho V_x V_y \\ (E + P + P_e)V_x\end{bmatrix} + \frac{\partial}{\partial y}\begin{bmatrix}\rho V_y \\ \rho V_y V_x \\ \rho V_y V_y + P + P_e \\ (E + P + P_e)V_y\end{bmatrix} = 0. \tag{9}$$

## 2. Numerical scheme and wave model

In order to solve the conservative form of the partially ionized plasma equations, the solution domain is divided into structured or unstructured triangles, as shown in Fig. 1. Thus Eq. (8) is integrated over the triangles and the solutions are obtained on their nodes. The resulting scheme is given by

$$\int_T \frac{\mathbf{U}^{n+1} - \mathbf{U}^n}{\Delta t}\,\mathrm{d}S = \Phi_T = -\int_{S_T} \nabla \cdot \vec{\mathbf{F}}\,\mathrm{d}S = -\int_{S_T} (\mathbf{F}_x + \mathbf{G}_y)\,\mathrm{d}S, \tag{10}$$

where $\vec{\mathbf{F}} = (\mathbf{F}, \mathbf{G})$ and $\Delta t$ is the time step which satisfies the CFL condition according to the fastest wave in the system. In addition, $\Phi_{\mathrm{T}}$ is the flux divergence and is named the total fluctuation, i.e., the sum of the

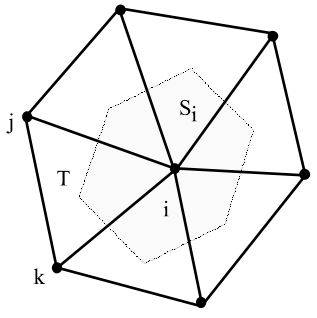


Fig. 1. The mesh structure. The nodes of triangle, T, are $i$, $j$, $k$ and $S_i$ is the median dual cell area surrounding node $i$.

individual wave fluctuations as a function of eigenvalues, eigenvectors and strengths of the possible waves in the wave pattern of the system.

### 2.1. The wave model: ION-A

In order to solve above system of equations, a new wave model (called ION-A) is constructed. To describe the derivation of ION-A and the underlying numerical solution technique, Eq. (8) is written in primitive form given by

$$\frac{\partial \mathbf{W}}{\partial t} + A\frac{\partial \mathbf{W}}{\partial x} + B\frac{\partial \mathbf{W}}{\partial y} = 0, \tag{11}$$

where $\mathbf{W} = [\rho, V_x, V_y, P]^{\mathrm{T}}$ is the primitive state vector and $A$ and $B$ are primitive Jacobian matrices. The eigenvalues of this system are the same as those of conservative one and their eigenvectors can easily be transformed into the conservative ones by means of $U_w = \partial\mathbf{U}/\partial\mathbf{W}$, the conservative to primitive state Jacobian matrix. The primitive equations (in detail) used in the derivation of ION-A are

$$\frac{\partial \mathbf{W}}{\partial t} + \begin{bmatrix} V_x & \rho & 0 & 0 \\ \frac{\alpha_\rho P}{\rho} & V_x & 0 & \frac{\beta}{\rho} \\ 0 & 0 & V_x & 0 \\ 0 & \Psi & 0 & V_x \end{bmatrix} \frac{\partial \mathbf{W}}{\partial x} + \begin{bmatrix} V_y & \rho & 0 & 0 \\ 0 & V_y & 0 & 0 \\ \frac{\alpha_\rho P}{\rho} & 0 & V_y & \frac{\beta}{\rho} \\ 0 & \Psi & 0 & V_y \end{bmatrix} \frac{\partial \mathbf{W}}{\partial y} = 0, \tag{12}$$

where $\alpha_P = \frac{\partial \alpha}{\partial P} = -f[3/(2P) + \rho\Theta_{\mathrm{ion}}/P^2]$, $\alpha_\rho = \frac{\partial \alpha}{\partial \rho} = -f[5/(2P) + \Theta_{\mathrm{ion}}/P]$ and $f = Z/2 - \sqrt{Z}/2(Z+2)/\sqrt{Z+4}$, $\beta = 1 + \alpha + P\alpha_P$ and $\Psi = \gamma P\zeta_e$ where

$$\zeta_e = \frac{1 + P\alpha_P + 2/5\rho\alpha_\rho(1 - \Theta_{\mathrm{ion}}/T_e)}{\beta + 2/3\rho\Theta_{\mathrm{ion}}\alpha_P} \tag{13}$$

for $\gamma = 5/3$. Notice that, when electronic effects are neglected $\Psi$ vanishes (i.e., $\alpha \to 0$, $\alpha_P$, $\alpha_\rho \to 0$, and $\zeta_e \to 0$) so that Eq. (12) turn into Euler equations.

Eqs. (12) are hyperbolic in nature and their eigen-system displays a wave character. To determine the wave solution, it is assumed that $\mathbf{W} = \mathbf{W}(\chi)$ where $\chi = \vec{x}\cdot\vec{n}_\theta - \lambda_\theta t$ is the phase of the wave front that moves in the direction of $\vec{n}_\theta$. Note that different waves are allowed to propagate in different directions, i.e., $\vec{n}_\theta^k$ for wave, $k$. Inserting this into Eq. (11) results in

$$[-\lambda_\theta I + An_x + Bn_y]\frac{\partial \mathbf{W}}{\partial \chi} = 0, \tag{14}$$

where $n_x$ and $n_y$ are $x$ and $y$ components of $\vec{n}_\theta$. It is clear from this equation that, $\lambda_\theta I$ is $4\times 4$ diagonal matrix of the eigenvalues of $A_n = An_x + Bn_y$ and $\partial\mathbf{W}/\partial\chi$ is its eigenvector (note that it is $A_n$ from which the wave model: ION-A presented here is developed). Thus, the gradient (i.e., $x$ and $y$ derivatives) of $\mathbf{W}$ may be written in terms of the right eigenvectors of $A_n$ as

$$\nabla\mathbf{W} = \sum_{k=1}^{N} \alpha_k r_w^k \vec{n}_\theta^k, \tag{15}$$

where the coefficient $\alpha_k$ is the strength of the $k$th wave and $r_w^k$ is its right eigenvector. This equation results in the change in conservative state as

$$\nabla\mathbf{U} = \sum_{k=1}^{N} \alpha_k r_u^k \vec{n}_\theta^k, \tag{16}$$

where $N$ is the total number of waves and as stated before, $r_u^k = r_w^k U_w$ can be used to obtain conservative right eigenvectors from the primitive ones. Thus, the change in conservative fluxes (i.e., the fluctuation defined in Eq. (10) becomes

$$\Phi_T = -\int_{S_T} \nabla \cdot \vec{\mathbf{F}}\, \mathrm{d}S = \sum_k D_k^{\mathrm{T}} \Phi_k, \tag{17}$$

and the update of the solution at the node $i$ of T, given by Eq. (10), turns into

$$\mathbf{U}_i^{n+1} = \mathbf{U}_i^n + \frac{\Delta t}{S_i} \sum_{T \in i} \sum_k D_k^{\mathrm{T}} \Phi_k, \tag{18}$$

where

$$\Phi_k = -S_T \lambda_k \alpha_k r_u^k \tag{19}$$

is the wave fluctuation and $D_k^{\mathrm{T}}$ is the matrix of distribution parameters satisfying $D_i + D_j + D_k = I$ where $i, j, k$ are the nodes of triangle T, see Fig. 1. Note that the directions of the waves determine the form of these distribution parameters. If the direction is towards the node $i$, then $D_i = I$ while $D_j = D_k = 0$, this is called one node update since only the state at this node is updated. When the direction is towards two nodes, say $i, j$ then $D_k = 0$ and $D_i$ and $D_j$ must be carefully selected. Ref. [4] explains in detail how this is done.

From Eq. (12) it is evident that the matrix $A_n$ is given as

$$A_n = \begin{bmatrix} V_n & \rho n_x & \rho n_y & 0 \\ \alpha_\rho P/\rho n_x & V_n & 0 & \beta/\rho n_x \\ \alpha_\rho P/\rho n_y & 0 & V_n & \beta/\rho n_y \\ 0 & \Psi n_x & \Psi n_y & V_n \end{bmatrix}, \tag{20}$$

where now

$$\Psi = \frac{\gamma P(1 + \alpha - 3/5\rho\alpha_\rho(1 + z/3))}{1 + \alpha + P\alpha_P(1 + z/3)} \tag{21}$$

with $z = 2\Theta_{\mathrm{ion}}/T_e$ and again $\gamma = 5/3$. The eigenvalues of this matrix are

$$\Lambda = V_n, V_n, V_n - a, V_n + a, \tag{22}$$

where $V_n = n_x V_x + n_y V_y = \cos\theta V_x + \sin\theta V_y$ and $a$ is the generalized sound speed given by

$$a = \sqrt{\beta\Psi/\rho + P\alpha_\rho}. \tag{23}$$

The first two waves denote the entropy and entropy-vortex waves while the last two represent backward and forward acoustic waves. Note that, as the electronic contributions are neglected (i.e., $\alpha \to 0$, $\alpha_P$, $\alpha_\rho \to 0$ so that $\Psi \to \gamma P$), this sound speed approaches, $a = a_0 = \sqrt{\gamma P/\rho}$, the classical sound speed.

The right eigenvectors of $A_n$ that is given by Eq. (20) are given by the following matrix:

$$R_w = \begin{bmatrix} 1 & 0 & \rho/A & \rho/A \\ 0 & -n_y & -n_x & n_x \\ 0 & n_x & -n_y & n_y \\ -P\alpha_\rho/\beta & 0 & \Psi/A & \Psi/A \end{bmatrix}, \tag{24}$$

where the columns of $R_w$ represent, entropy, entropy-vortex, backward and forward acoustic waves respectively. The wave-strengths of these waves are found by solving Eq. (15) for $\alpha_k$ provided that the $x$–$y$ derivatives of $\mathbf{W}$ are known on the triangle. Since Eq. (15) provides a total of 8 derivatives, it is made of 8

equations. Unfortunately, assuming 4 waves with 4 different propagation angles (this is the ideal case for minimum numerical dissipation) requires the solution of nonlinear equations. In order to handle this problem, the number of propagation angles is reduced and the number of waves is increased. This extra dissipation causes a spread of the discontinuities and shocks but the system of equations to be solved becomes relatively easy. Using this idea (see [4]), Eq. (15) with 6 waves is written as

$$(\mathbf{W}_x, \mathbf{W}_y) = \alpha_1 r_{w1}(\cos\theta_e, \sin\theta_e) + \alpha_2 r_{w2}(\cos\theta, \sin\theta) + \sum_{s=3}^{4} \alpha_s r_{ws}(\cos\theta, \sin\theta) + \sum_{s=5}^{6} \alpha_s r'_{ws}(\cos\theta', \sin\theta'), \tag{25}$$

where the first two waves are entropy and entropy-vortex, waves and others are acoustic waves. $\theta_e$ is the propagation angle of the entropy wave and $\theta$ (and $\theta' = \theta + \pi/2$) is the propagation angles of the other waves. As seen, having 6 strengths and 2 different angles leads to 8 unknowns and one has a consistent set of equations. Note that $r'_{ws}$ are the eigenvectors of the additional two waves propagating in perpendicular to the original acoustic waves and they can be found by interchanging $\theta$ by $\theta + \pi/2$ in Eq. (24). These wave-strengths and wave propagation angles are given by

$$\alpha_1 = \frac{a_0^2}{A^2}\beta\sqrt{X_e^2 + Y_e^2}, \quad \theta_e = \tan^{-1}(Y_e/X_e), \tag{26}$$

$$\alpha_2 = V_{y,x} - V_{x,y}, \quad \theta = \frac{1}{2}\tan^{-1}\left(\frac{V_{x,y} + V_{y,x}}{V_{x,x} - V_{y,y}}\right), \tag{27}$$

$$\alpha^{3,4} = \frac{1}{2}\left[\mp\frac{1}{2}(\nabla\cdot\mathbf{V} + D) + \frac{1}{\rho A}\nabla P^{\mathrm{T}}\cdot\vec{n}_\theta\right], \tag{28}$$

$$\alpha^{5,6} = \frac{1}{2}\left[\mp\frac{1}{2}(\nabla\cdot\mathbf{V} - D) + \frac{1}{\rho A}\nabla P^{\mathrm{T}}\cdot\vec{n}'_\theta\right], \tag{29}$$

where

$$X_e = \zeta\rho_x - \frac{P_x}{a_0^2}, \quad Y_e = \zeta\rho_y - \frac{P_y}{a_0^2}, \quad \zeta = \frac{1 + P\alpha_P + 2\rho\alpha_\rho/5P(P - \rho\Theta_{\mathrm{ion}})}{\beta + 2/3\rho\Theta_{\mathrm{ion}}\alpha_P}$$

and $D = \sqrt{(V_{x,y} + V_{y,x})^2 + (V_{x,x} - V_{y,y})^2}$, $P^{\mathrm{T}} = P + P_e$ being the total pressure. Note that in the above equations, the second subscripts denote derivatives.

### 2.2. Initial conditions

As a test-case for the numerical scheme presented above, the stability of hypersonic and ionizing shock waves is examined. To do that, a rectangular region is divided into 2 domains and an initial stationary shock solution (obtained from the Rankine–Hugoniot relations in the reference frame of moving shock) is given as the initial condition. The problem is then run for very long times in order to check whether the scheme keeps the locations and the strengths of the initial shock unchanged. The shock stability is also investigated by perturbing the shock front by small amplitude waves moving towards the shock at different angles.

Thus, it is assumed that a hypersonic shock moves, in the positive $x$-direction, into a stationary ($\mathbf{V} = 0$) and not ionized region characterized by the physical quantities defined as pre-shock values: $T_0 = 300$ K, $P_0 = 5$ Torr $= 666.5$ Pa (thus $\rho_0 = P_0/T_0 = 0.00774\ \mathrm{kg/m^3}$ and the constant $b_0$ in Eq. (7) becomes $b_0 = 857.6$). Since no pre-shock ionization is considered (i.e., $\alpha = 0$ and $P_{e0} = 0$) this region satisfies the Euler equations for ideal and non-viscous gas. The region behind the shock includes a partially ionized subsonic gas which should be investigated by high temperature gas dynamics including electronic effects.

The code presented here automatically handles the cases in which ionization is not negligible. The electronic effects are included in the equation of state through Saha equation which is used to calculate the ionization degree, $\alpha$.

### 2.3. Rankine–Hugoniot conditions

The Rankine–Hogoniot (RH) conditions are formulated in a frame of reference in which the shock is stationary. These conditions can be obtained by equating the conservative fluxes on both sides of the stationary shock:

$$\begin{bmatrix} \rho V'_n \\ \rho V'_n V'_n + P + P_e \\ \rho V'_n V'_\perp \\ (E + P + P_e) V'_n \end{bmatrix}_{\text{left}} = \begin{bmatrix} \rho V'_n \\ \rho V'_n V'_n + P + P_e \\ \rho V'_n V'_\perp \\ (E + P + P_e) V'_n \end{bmatrix}_{\text{right}}, \tag{30}$$

where $V'_n = V_x - V_{x,\text{shock}}$ is the velocity normal to the shock surface and $V'_\perp = V_y - V_{y,\text{shock}}$ is the tangential velocity along the shock surface (note that the primed velocities are those in shock's reference frame and $V_{\text{shock}}$ is the shock velocity. When the shock motion is in $+x$ direction (i.e., $V_{y,\text{shock}} = 0$) into a non-ionizing region on the right, one has the typical behaviour in the laboratory frame and shock frame as shown in Fig. 2. In order to derive the RH relations (or shock adiabatic) between the initial right and left state around the stationary shock surface, the following dimensionless physical quantities are defined:

$$\eta = \frac{\rho_{\text{L}}}{\rho_0}, \quad P = \frac{P_{\text{L}} + P_{e\text{L}}}{P_0}, \quad \Theta = \frac{T_{\text{L}}}{T_0}, \tag{31}$$

where $\eta$ is the density ratio while $P$ and $\Theta$ are total pressure and temperature ratios respectively. Using these definitions, the shock speed can be found as

$$V_{\text{shock}} = \left[\frac{P_0}{\rho_0}\frac{\eta}{\eta - 1}(P - 1)\right]^{\frac{1}{2}}, \tag{32}$$

and the RH conditions turn into the following relations between the density, pressure, and temperature ratios:

$$\eta = \frac{1 + 4P}{4 + P - 2\alpha\Theta_{\text{ion}}/T_0}, \quad P = (1 + \alpha)\eta\Theta, \quad \alpha = \frac{1}{2}\left[-Z + \sqrt{Z^2 + 4Z}\right], \tag{33}$$

where $Z = b_0\left(\frac{\Theta^{3/2}}{\eta}\right)\exp\left(-\frac{\Theta_{\text{ion}}}{\Theta}\right)$. The values $\rho_0 = 1$, $T_0 = 1$, $P_0 = 1$, $\alpha = 0$, $P_e = 0$ were taken as the state values for the stationary region on the right, and for each given value of temperature ratio, $\Theta$, the implicit Eqs. (33) and (32) were solved numerically in order to obtain the corresponding other quantities (i.e., $\eta$ and $\Theta$).

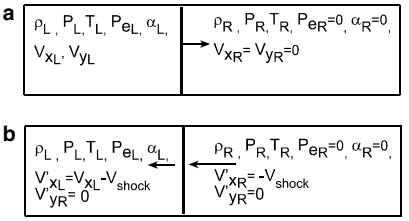


Fig. 2. (a) The hypersonic shock front moving right into the non-ionized region leaving behind a partially ionized region with high temperatures (initial RH conditions); (b) what happens in shock's reference frame.

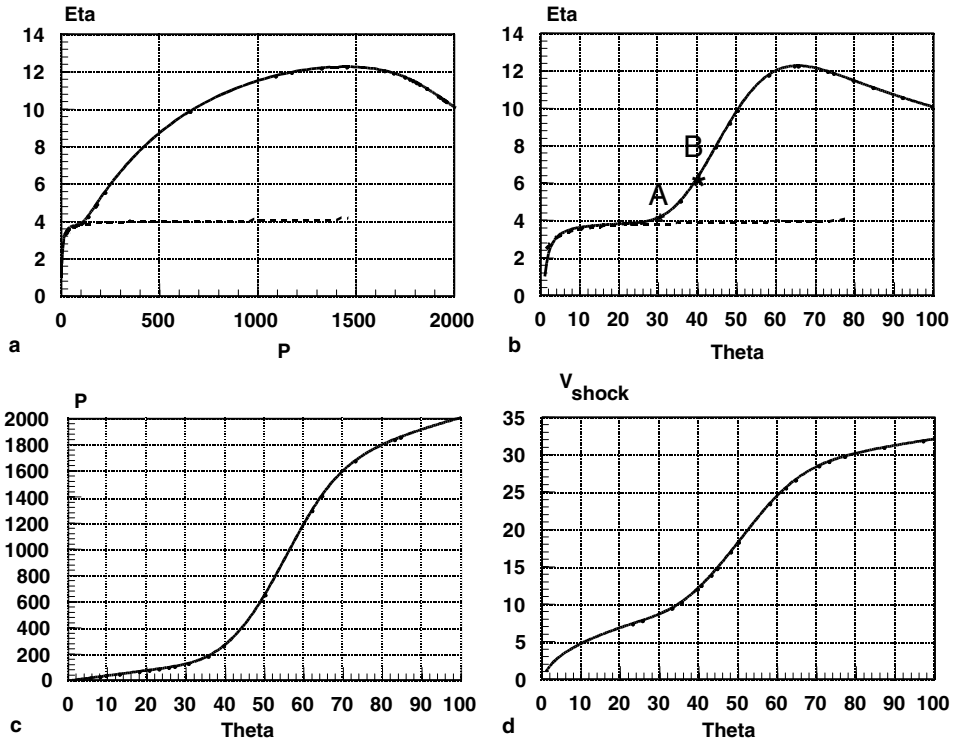


Fig. 3. The initial RH solutions among the density, pressure, and temperature jump (i.e., $\eta$, $P$, $\Theta$). The shock adiabatic is given by (a).

Fig. 3 shows the resulting relationships among the density, pressure, and temperature jumps obtained by this procedure (note that the shock adiabatic is given by Fig. 3(a) and it is the same as that given in [2]). The dotted lines in the first two graphs correspond to classical gas dynamic case and points A and B correspond to the two sample test-cases considered in this work.

## 3. Numerical solution procedure

Recently, many journal articles describing multi-dimensional upwinded solvers for both the Euler equations and the MHD equations have been generated, see [10–14]. Although, the finite volume (FV) formulations are the schemes [10] widely used for the numerical methods, the fluctuation splitting (FS) schemes [11] have also been used successfully. The FS schemes differ from the FV schemes in the sense that the flow variables are not mesh averages but are kept at the vertices of the mesh and that the numerical fluxes are not used. See [15] for a comparison between the FS and FV schemes.

In the FS scheme developed here, the conservative state is solved on structured or unstructured triangular meshes by utilizing the new wave model: ION-A. Note that several wave models have been developed for the Euler equations [5] and for the MHD equations [1,4]. As done with other wave models, ION-A is utilized to calculate the individual fluctuations of possible waves, by first determining their effects due to the gradients in the physical variables, and then distributing them to the nodes of triangles in an upwind manner. As it was explained earlier, the time rate of the conservative state given by Eq. (10) turns into Eq. (18) as a function of the eigen-system of conservative Jacobian matrices. This eigen-system (evaluated in each

triangle, T) requires the values of mesh averaged primitive variables, and their gradients. The area integral of the Jacobian matrices is very complicated due to the fact that their elements are nonlinearly dependent on the primitive state, **W**. In order to circumvent this difficulty, another state vector, **Z** (parameter state) is introduced with the requirement that it varies linearly in $T$ and the elements of **U**, **W**, **F**, and **G** are quadratic in the components of **Z**. In that case $\partial\mathbf{U}/\partial\mathbf{Z}$, $\partial\mathbf{W}/\partial\mathbf{Z}$, $\partial\mathbf{F}/\partial\mathbf{Z}$, and $\partial\mathbf{G}/\partial\mathbf{Z}$, are linear in **Z**, thus their surface integrations may be evaluated by the average parameter vector, $\overline{\mathbf{Z}}$, see [5] for similar Eulerian models.

### 3.1. Solution algorithm

For each triangle, T:

1. find $\rho$, $V_x$, $V_y$, $P$ from the conservative state vector by employing a Newton type algorithm for pressure and obtain $\mathbf{Z} = [\sqrt{\rho}, \sqrt{\rho}V_x, \sqrt{\rho}V_y, \sqrt{\rho}H_{\mathrm{T}}]^{\mathrm{T}}$, the parameter state, for each node $i$ of T,
2. using 3 nodal values of T, find the mesh averaged parameter vector, and its gradient from

$$\overline{\mathbf{Z}} = \frac{1}{3}\sum_{m=1}^{3}\mathbf{Z}_m, \quad \nabla\mathbf{Z} = \frac{1}{2S_T}\sum_{m=1}^{3}\vec{n}_m\mathbf{Z}_m, \tag{34}$$

3. using the matrix: $\partial\mathbf{W}/\partial\mathbf{Z}$ determine the average primitive state given as $\mathbf{W} = [\overline{\rho}, \overline{V}_x, \overline{V}_y, \overline{P}]^{\mathrm{T}}$ with a Newton type algorithm for average pressure,
4. obtain the $x$ and $y$ derivatives of **W** noting the fact that an implicit equation is to be inverted to get $P_x$ and $P_y$ (since $\alpha = f(\rho, P)$),
5. using these averages, evaluate $\overline{Z}, \overline{\alpha}, \overline{\alpha}_\rho, \overline{\alpha}_P, \overline{\Psi}, \overline{\beta}$ and get the averaged sound speed $\overline{a}$ from Eq. (23),
6. find the eigenvalues from Eq. (22), the propagation angles $\theta_e$ and $\theta$ from Eqs. (26) and (27) and obtain the wave-strengths from Eqs. (26)–(29); then get the right primitive eigenvectors, $\overline{r}_w$ from Eq. (24), and the conservative eigenvectors, $\overline{r}_u$ using the matrix: $\partial\mathbf{U}/\partial\mathbf{W}$,
7. having determined the eigen-system of 6 individual waves for each wave, $k$
   7.1. get the wave fluctuation from Eq. (19) using the averaged values: $\overline{\lambda}_k$, $\overline{\alpha}_k$ and $\overline{r}_u^k$,
   7.2. using the mesh properties and $\vec{n}(\theta) = (\cos\theta, \sin\theta)$, determine the upwind nodes for this wave and assign $\overline{\Phi}_k$ to these nodes of T using the distribution technique described in [1] or [5].

After the contributions of each wave $k$ are obtained at the nodes of the triangles and all the triangles around nodes are visited, the nodal mesh updates will have been completed and the nodal values will have reached their values at the new time step, $n + 1$, see Eq. (18).

In this work, the time update given by Eq. (18) was carried out by third order Runge–Kutta (RK) method for improved time accuracy of the scheme. This third order accurate RK method which is positive and oscillation free is given by [9]

$$\begin{aligned}
\mathbf{U}^1 &= \mathbf{U}^n + \Delta t\,\mathrm{Res}(\mathbf{U}^n),\\
\mathbf{U}^2 &= \frac{3\mathbf{U}^n + \mathbf{U}^1}{4} + \frac{\Delta t}{4}\,\mathrm{Res}(\mathbf{U}^1),\\
\mathbf{U}^{n+1} &= \frac{\mathbf{U}^n + 2\mathbf{U}^2}{3} + \frac{2\Delta t}{3}\,\mathrm{Res}(\mathbf{U}^2).
\end{aligned} \tag{35}$$

Before turning to the numerical results few comments on the numerical procedure are due:

### 3.2. Newton iterations for equation of state

Since, the primitive variables: $\mathbf{W} = [\rho, V_x, V_y, P]^{\mathrm{T}}$ are used to obtain the eigen-system, they must be calculated correctly from the conservative variables: $\mathbf{U} = [\rho, \rho V_x, \rho V_y, E]^{\mathrm{T}}$ at each time iteration. It is easy to get the velocities from the density and momenta. When classical gas dynamics is considered the pressure may be calculated explicitly from the equation of state and the expression for the internal energy. However, in the case presented here, the total energy is a nonlinear function of pressure, as is clearly seen in Eqs. (5) and (6). Hence both the pressure as well as the ionization degree must be obtained simultaneously by employing a root solver algorithm (such as Newton's) provided that the density, velocity, and total energy are known. Since $P_e = \rho\alpha T$, the total energy can be written as

$$E = \frac{1}{2}\rho\mathbf{V}^2 + \frac{\rho T(1+\alpha)}{\gamma - 1} + \rho\alpha\Theta_{\mathrm{ion}}, \tag{36}$$

where $\alpha$ is given by Eq. (6) and $Z$ is given by Eq. (7). Thus for given $E$, $\rho$, and $\mathbf{V}$, the function whose root is sought is

$$F = E - \left[\rho\alpha\Theta_{\mathrm{ion}} + (1+\alpha)\frac{P}{\gamma - 1} + \frac{1}{2}\rho V^2\right]. \tag{37}$$

Newton's algorithm is then is given by

$$P^{k+1} = P^k - \frac{F^k}{F'}, \tag{38}$$

where '$k$' is the iteration level and

$$F' = -\frac{1+\alpha^k}{\gamma - 1} - \left[\frac{P^k}{\gamma - 1} + \rho\Theta_{\mathrm{ion}}\right]\alpha_P^k, \tag{39}$$

where $F'$ and $\alpha_P$ are the derivatives of $F$ and $\alpha$ with respect to $P$ respectively. As known, Newton's method is generally guaranteed to converge if the initial guess is sufficiently close to the solution. If the initial guess, $P^0$, is obtained from the previous time step, $P^{k+1}$ approaches correct pressure as iterations converge within a prescribed tolerance.

### 3.3. Newton iterations for averages

The parameter state for this work was chosen to be

$$Z = [Z_1, Z_2, Z_3, Z_4]^{\mathrm{T}} = [\sqrt{\rho}, \sqrt{\rho}V_x, \sqrt{\rho}V_y, \sqrt{\rho}H_{\mathrm{T}}]^{\mathrm{T}}, \tag{40}$$

where $H_{\mathrm{T}} = (E + P + Pe)/\rho$ is the total enthalpy. If is given by the same as Eq. (40) (with elements are averaged) one can get $\overline{\rho}$ and $\overline{\mathbf{V}}$ from $\overline{\rho} = \overline{Z}_1^2$, $\overline{V}_{x,y} = \overline{Z}_{2,3}/\overline{Z}_1$, and $\overline{H}_{\mathrm{T}} = \overline{Z}_4/\overline{Z}_1$. Note that to get $\overline{P}$ from $\overline{\mathbf{Z}}$, one must follow similar root finding procedure that was described before. To do that the iteration given by Eq. (38) is used with

$$F^k = \frac{\gamma}{\gamma - 1}(1+\alpha_k)P^k - \overline{\rho}\overline{H}_{\mathrm{T}} + (\overline{\rho}\alpha^k\Theta_{\mathrm{ion}} + \overline{\rho}\overline{V}^2/2) \tag{41}$$

and

$$F' = \frac{\gamma}{\gamma - 1}(1+\alpha_k) + \left[\frac{\gamma}{\gamma - 1}P^k + \overline{\rho}\Theta_{\mathrm{ion}}\right]\alpha_P^k. \tag{42}$$

As iterations converge, the average pressure (and hence average $\alpha$) is obtained. This procedure is followed for each visited triangle, T in which the individual fluctuations are calculated and distributed to its nodes.

### 3.4. Gradients of physical variables

The gradients of the physical variables in 'T' are obtained by using

$$(\rho)_{x,y} = 2\overline{Z}_1(Z_1)_{x,y}, \quad (V_x)_{x,y} = (\overline{Z}_2)_{x,y}/\overline{Z}_1 - \overline{Z}_2/\overline{Z}_1^2(Z_1)_{x,y},$$
$$(V_y)_{x,y} = (\overline{Z}_3)_{x,y}/\overline{Z}_1 - \overline{Z}_3/\overline{Z}_1^2(Z_1)_{x,y}, \quad (P)_{x,y} = \sum_{j=1}^{4} T_j(Z_j)_{x,y} \tag{43}$$

where

$$T_1 = (1+\overline{\alpha})[\overline{Z}_4 - 2\overline{Z}_1(\overline{\alpha}\Theta_{\text{ion}} + \zeta\overline{\alpha}_P)], \; T_{2,3} = -\gamma'(1+\overline{\alpha})/[1+\gamma'(1+\overline{\alpha})\zeta\overline{\alpha}_P]\overline{Z}_{2,3} \text{ and}$$
$$T_4 = \gamma'(1+\overline{\alpha})/[1+\gamma'(1+\overline{\alpha})\zeta\overline{\alpha}_P]\overline{Z}_1$$

where $\gamma' = (\gamma-1)/\gamma$ and $\zeta = \overline{\rho}\Theta_{\text{ion}} + (\rho\overline{H}_{\text{T}} - \overline{V}^2/2 - \overline{\rho\alpha}\Theta_{\text{ion}})/(1+\overline{\alpha})$. Notice that, $T_1$–$T_4$ are obtained from the elements of the matrix: $\partial\mathbf{W}/\partial\mathbf{Z}$ provided that $\alpha = \alpha(\rho, P)$ being nonlinearly dependent on $\rho$ and $P$. In addition, the gradient of electron temperature can be calculated from: $(T_e)_{x,y} = (P)_{x,y}/\overline{\rho} - \overline{P}/\overline{\rho}^2(\rho)x, y$.

## 4. Numerical results

### 4.1. Sod's shock tube test ($\gamma = 1.4$)

This purely hydrodynamic test introduced in [6] involves a left moving fast rarefaction (FR−), a right moving contact discontinuity (CD+) and a fast shock (FS+) ahead of it. The initial data (with no ionization, i.e, $\alpha = 0$) was chosen as $\mathbf{W}^{\text{L}} = [1, 0, 0, 1]$, $\mathbf{W}^{\text{R}} = [0.125, 0, 0.1]$ and the problem was run until $t = 0.1$ on a highly elongated mesh with boundaries $x, y \in [0, 1]$. The resulting density profiles in $x$ direction (at $y = 0.5$) as a function of different mesh sizes ($100, 200, 800, 1600 \times 3$) are shown in Fig. 4(a). As seen from this convergence study, the solution shows no post shock oscillations and the contact and shock get sharper as the mesh resolution is increased. In Fig. 4(b), the resulting density and pressure profiles are presented

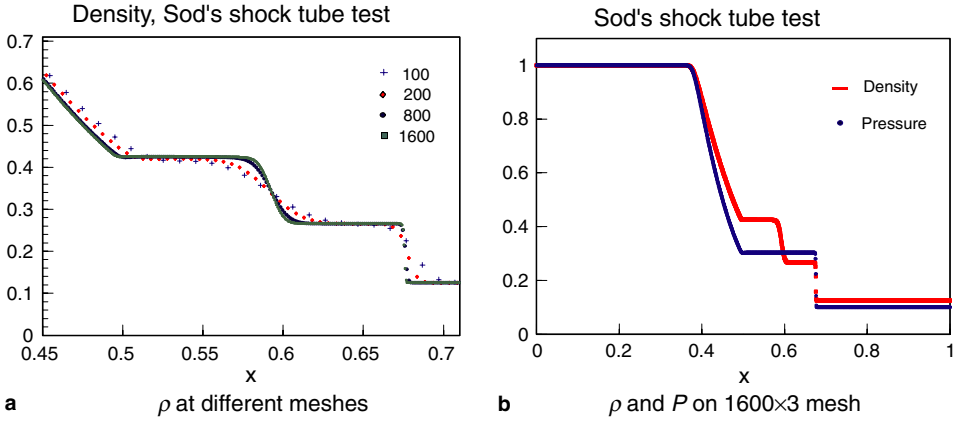


Fig. 4. Sod's shock tube test at $t = 0.1$, on $100, 200, 800, 1600 \times 3$ R-grid, $\gamma = 1.4$. Plots show FR−, CD+, FS+ from left to right.

obtained at $t = 0.1$ on the $1600 \times 3$ mesh. These results agree well with those presented in [6] showing that model ION-A reduces to the correct 1D limit as ionization degree vanishes (i.e., no electrons exist in the medium). No numerical efforts were taken to set ionization degree and $V_y$ to zero, although some negligible errors for these fields were observed near the shock and contact. In addition, for the coarser meshes, the shock seems to be slightly smeared right-biased. This issue should further be studied. Note also that these errors get smaller as the mesh is made finer.

### 4.2. Supersonic channel flow (Euler limit)

This test problem was chosen to check if the code presented here produces (automatically without employing some controlling parameters) regular gas dynamics (Euler) limit when the ionization degree is negligible. To show this, a supersonic channel flow is solved on a rectangular mesh which has a smoothly varying backward step (i.e. the bottom wall has a sine square profile: $y(x) = 0.2\sin^2[\pi(2 - x)/4]$ for $x < 2$ else $y = 0$). This test problem was considered in [7] for the solutions of Euler's equations. The domain considered is $x \in [0, 6]$, $y \in [0, 1]$, and a typical mesh is shown in Fig. 5. A uniform supersonic horizontal inflow into the non-ionized region is imposed at the $x = 0$ boundary with

$$v_x = 2\sqrt{\gamma}, \quad v_y = 0, \quad \rho = 1, \quad P = 1, \quad \gamma = 5/3.$$

The inflow Mach numbers is thus $M = 2$ so that the inflow is supersonic. At the bottom and top boundaries the ideal wall symmetry conditions are imposed by just modifying the velocity at this boundary such that its normal component vanishes. The fluid is allowed to flow out freely at $x = 6$, where the flow is supersonic. The resulting steady state density and Mach number color graphs in Fig. 6 as a function of different grids. The grids considered for this test were $71 \times 11$, $141 \times 21$, and $281 \times 41$ and a typical mesh is shown in Fig. 5. The solutions agree very well with those given in [7] and, as seen from the color graphs, the solution converges and the shocks become sharper as the grid is made finer.

As a convergence study, the density profiles at $y = 0.3$ and $y = 0.7$ are presented in Fig. 7 as a function of $x$ and different grid resolutions. As seen from this figure, the solutions converge to correct solutions as the solution mesh is made finer. In addition, one can see from the density graphs at $y = 0.7$, the reflected shock from the upper boundary is as sharp as the incoming one, resolving the shocks within 4–6 points. These results show that the code presented here successfully converges to correct Euler limit when the ionization is negligible, i.e., $\alpha \to 0$.

### 4.3. Stationary ionizing shock

In this test problem, it is assumed that a hypersonic ionizing shock moves right in a non-ionized region (i.e., $\alpha = 0$, $\rho = P = T = 1$) leaving behind an ionized region with very high temperature and density. The

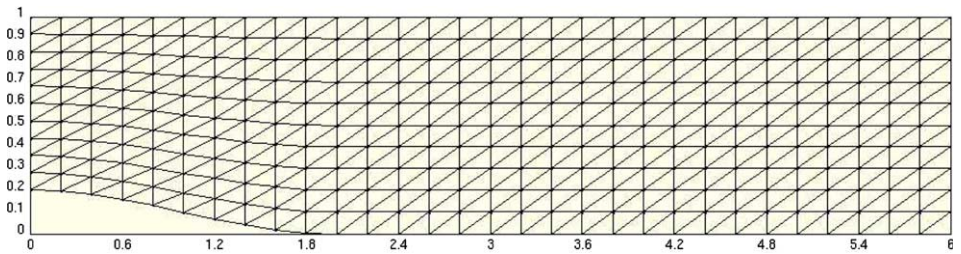


Fig. 5. A typical right running diagonal mesh used for supersonic channel flow test.

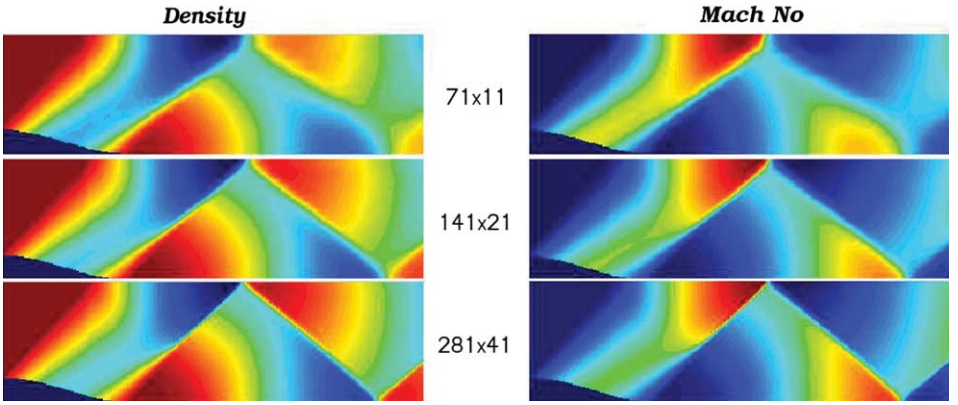


Fig. 6. Density and mach number color graph (on $77 \times 11$, $141 \times 21$, and $281 \times 41$ mesh.

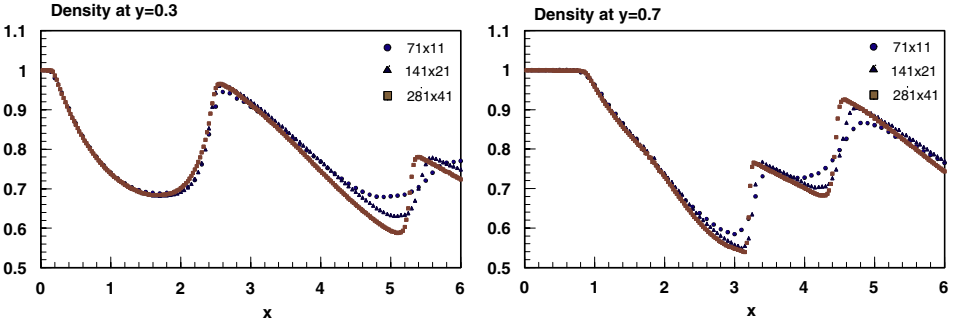


Fig. 7. The density $x$-profile at $y = 0.3$ and $y = 0.7$ for three different meshes: $71 \times 11$, $141 \times 21$, and $281 \times 41$.

temperature jump (i.e., $\Theta$) was chosen to be 30 (point A in Fig. 3(b)) and corresponding values of density, pressure, and $x$ velocity jumps were determined from the shock adiabatic given by Fig. 3. It is worthwhile to note that the Mach number for this case was 9.92. The resulting left state was found as: $\rho_L = 4.158$, $P_L = 124.764$, and $Vx_L = 9.729$ with a shock speed of 12.810 and ionization degree of $\alpha = 0.00701$. In order to obtain a stationary shock, the $x$ velocities on both sides of initial discontinuity were changed to $Vx_R = -12.810$ and $Vx_L = 9.729 - 12.810 = -3.081$, see Fig. 2(b). This problem was run for more that 30,000 time steps on highly elongated isotropic triangular mesh with free (outgoing) left and right boundaries. The density profile obtained initially and after 30,000 time steps on the $100 \times 3$ mesh are shown in Fig. 8 as a function of $x$. As seen, the shock remains stationary even after so many iterations. The log of L2 norm of the solutions until 10,000 time steps are shown in Fig. 9 for $100 \times 3$ and $1000 \times 3$ meshes. As seen, the error in the solutions reduce as the mesh is made finer and it remains within the same range after so many time steps. This behaviour repeats itself even after 30,000 time steps. The second test includes a stronger shock with a temperature jump of $\Theta = 40$ (point B in Fig. 3(b)) so that the Mach number is 13.97. According to the Hugoniot curves given in Fig. 3, this corresponds to a density jump of 6.33, a value that cannot be achieved by classical gas dynamics. Fig. 10(a) gives the resulting density profiles obtained at very early time and after 30,000 time steps on the same $100 \times 3$ mesh. As seen, the shock location remains unchanged as before but there is a slight increase in the density (i.e., $\eta = 6.5$ peaking at $\eta = 6.6$ instead of 6.33).

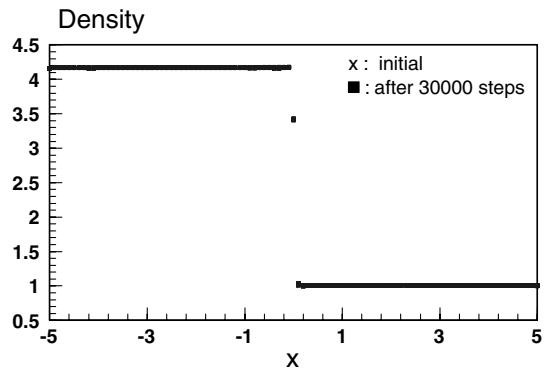


Fig. 8. The density profi ed initially and after 30,000 time steps from a hypersonic shock with a temperature jump of $\Theta = 30$.

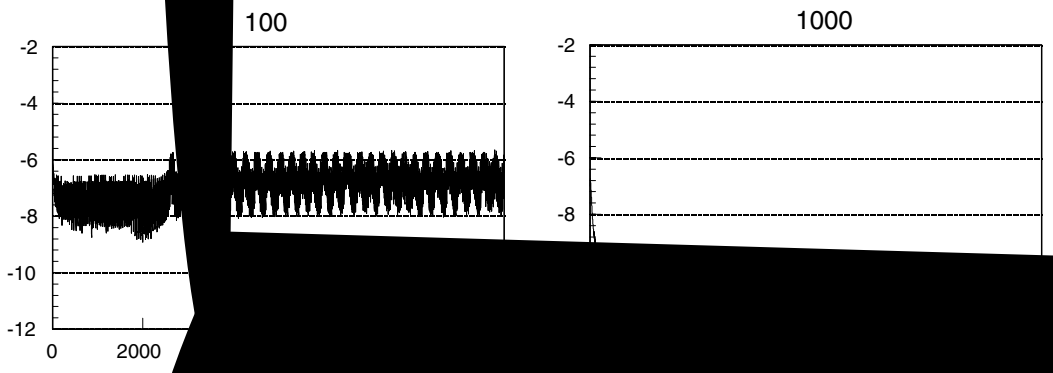


Fig. 9. The logarith

ensity

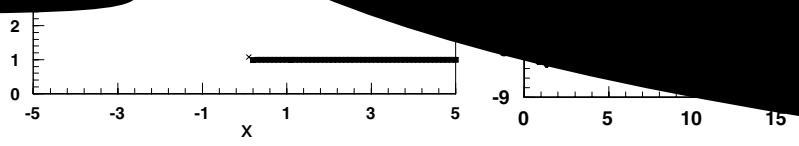

The reason of having unchanged shock location shows that the sound speed were calculated correctly in the code and RH conditions are satisfied reasonably. But the slight overshoot in the density (and hence in $\alpha$, etc.) results from numerical errors in the gradient and propagation angles. Fig. 10(b) gives the residual as a function of time. As seen the residual gets very small and remains constant at nearly $10^{-7}$ after $t = 5$. Fig. 11 shows the resulting density profile obtained on the $1000 \times 3$ mesh for $\Theta = 40$ case. In this case, the peak value of the density near the shock surface has dropped to 6.48 thus producing a better solution. This shows that as the grid is made finer, the errors arising from numerical errors in the gradient calculations get smaller, although the reduction is rather slow. This can be improved by employing higher order gradient calculations considering neighbor meshes.

### 4.4. Perturbed ionizing shocks

In this section, the stationary shock is perturbed at $t = 0$ in the following way:

$$f' = f(1 + \epsilon \sin ax \cos by), \tag{44}$$

where $f$ stands for the unperturbed physical variables (pressure, velocity, density) while $f'$ denote their perturbed values. The problem was run for 17,611 steps for $\epsilon = 0.1$, $a = 6/5\pi$, $b = 36\pi$, until $t = 11.48$. The resulting residual is presented on Fig. 12. As seen the residual remains extremely small for very long times, showing that the numerical scheme preserve the steady shock successfully. How the density and ionization degree change in time when the shock surface is perturbed are presented in Figs. 13 and 14 as color pictures. The density profiles at different times are plotted at the centerline (i.e., at $y = 0.5$) as a function of $x$ on Fig. 15. As seen from these figures, initial perturbation turns into parallel train of waves with different

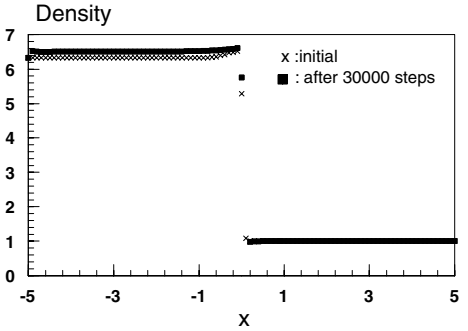


Fig. 11. The density profile obtained initially and after 30,000 time steps on $1000 \times 3$ mesh for $\Theta = 40$.

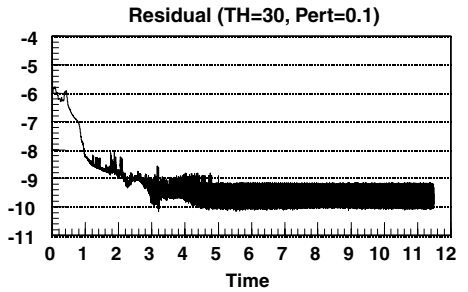


Fig. 12. The residual for perturbed shock surface on $200 \times 10$ mesh for $\Theta = 30$ case.

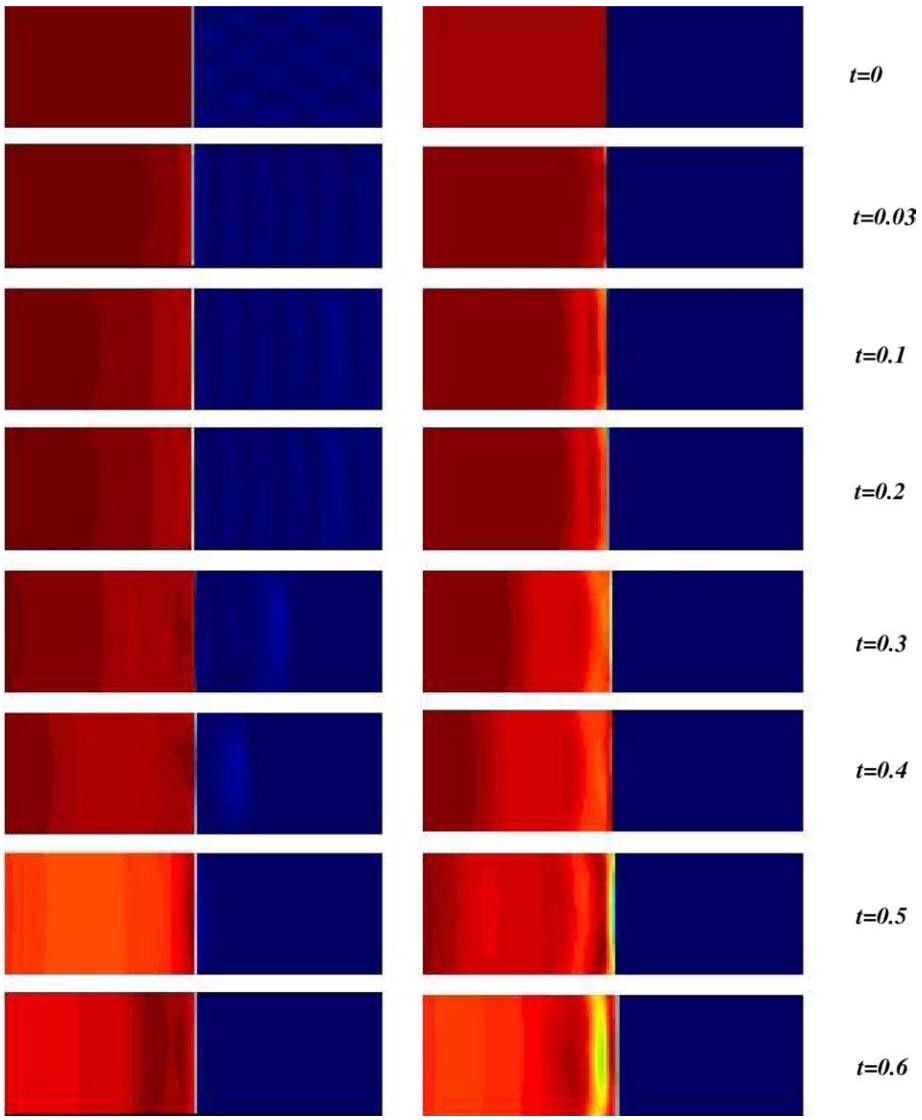


Fig. 13. Time evolution of perturbed shock on $200 \times 10$ mesh for $\Theta = 30$. Left and right columns show the density and ionization degree color graphs.

wavelength and strength which move towards the stationary shock at the center. Each perturbation wave creates their own effect on the shock and continue moving behind the shock. When the ionization values are examined one can see that the perturbation waves cause the ionization degree to increase behind the shock. Another noticeable effect is that the last perturbation wave which hit the shock surface at nearly $t = 5$ creates biggest perturbation and a pulse created in the ionization degree is forced to move in the ionized region behind the shock. This last perturbation reaches to the left boundary at nearly $t = 3$ and the shock surface reaches to steady state and remains at correct location and strength for very long times.

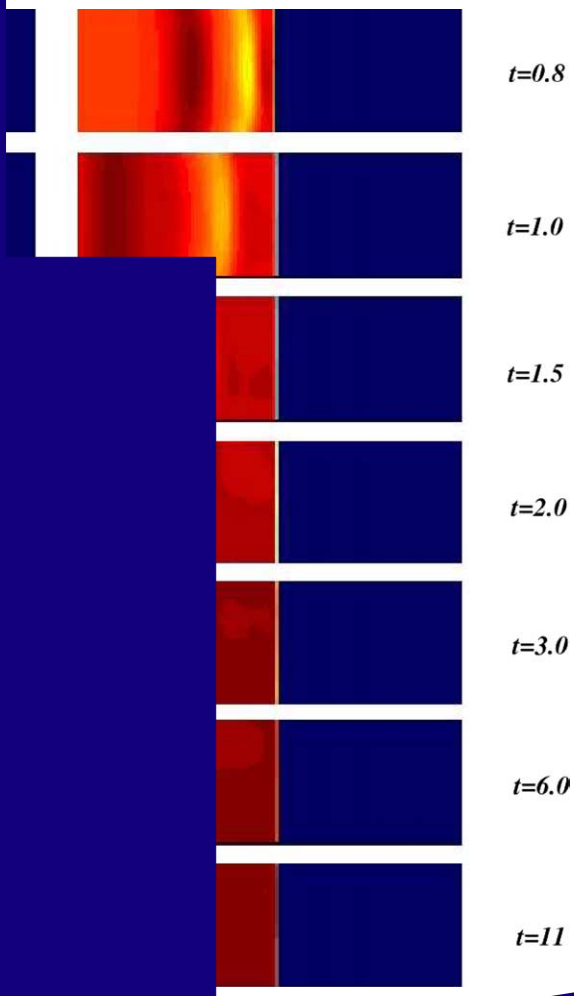


eft and right colum

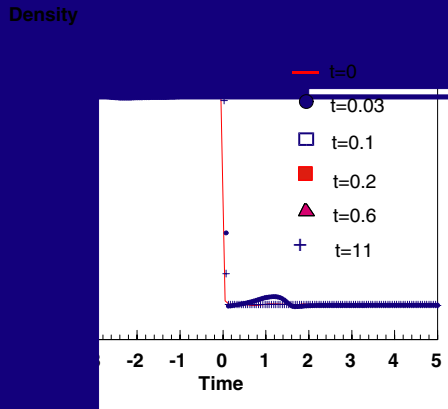


Fig. 15. Density profiles (as a function of $x$) for perturbation magnitude = 0.1 on $200 \times 10$ mesh for $\Theta = 30$ case.

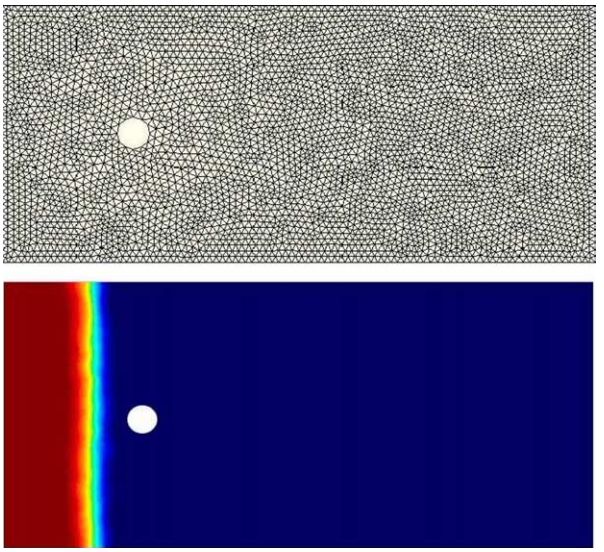

Fig. 16. The unstructured mesh with 2878 nodes and 5536 triangles used for the planar ionizing shock test and the initial location of ionizing shock approaching the circular obstacle from the left.

### 4.5. Interaction of a planar shock wave with a circular obstacle

In order to demonstrate the two-dimensional nature of ION-A, the flow that develops behind a planar shock wave propagating over a circular obstacle is examined in a rectangular region including a circular obstacle, see Fig. 16. As shown in Fig. 17, a planar shock wave propagates into an unperturbed cold gas that contains the circular obstacle. The temperature jump across the unperturbed shock is $\theta = 30$ and the corresponding values of the jumps in rest of the physical variables are given in Section 4.3. In Fig. 18 the shock is seen interacting with the obstacle while in Fig. 19 it is already moving to the right away from the obstacle. This sequence of three snapshots clearly indicates the robust stability of the shock. It

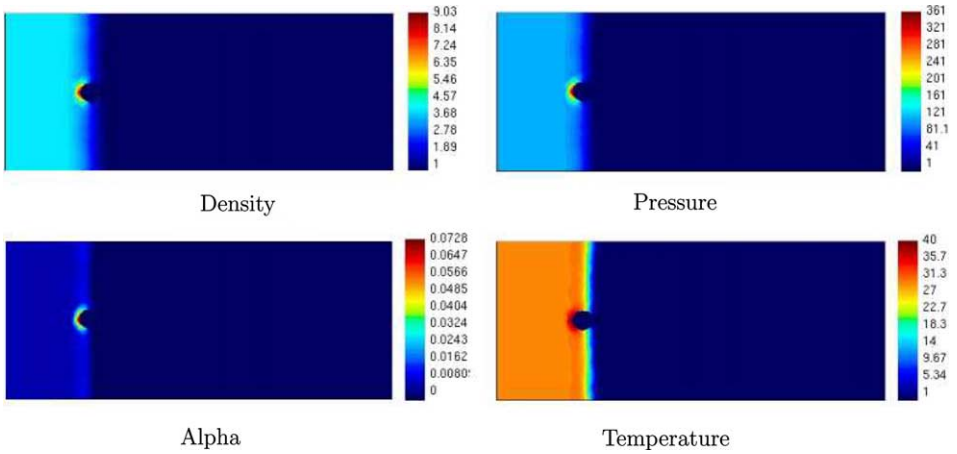


Fig. 17. Planar ionizing shock (with $\Theta = 30$) approaching the circular obstacle obtained on the mesh shown in Fig. 16.

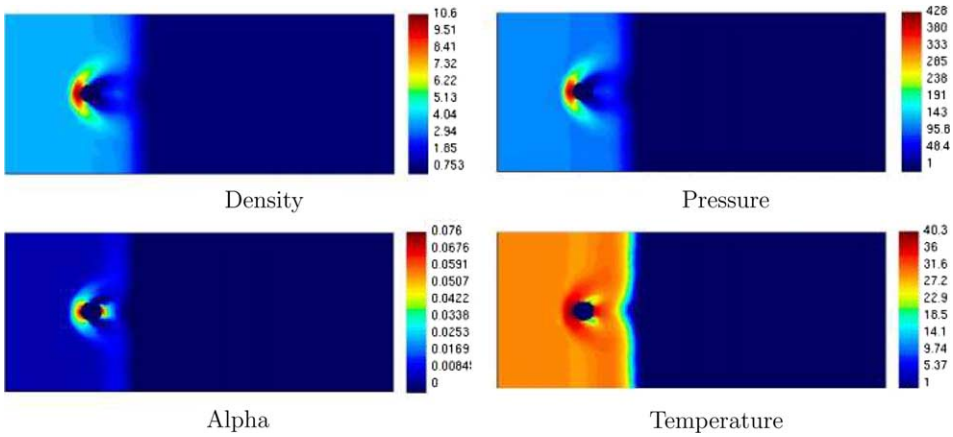


Fig. 18. Planar ionizing shock (with $\Theta = 30$) interacting with the circular obstacle obtained on the mesh shown in Fig. 16.

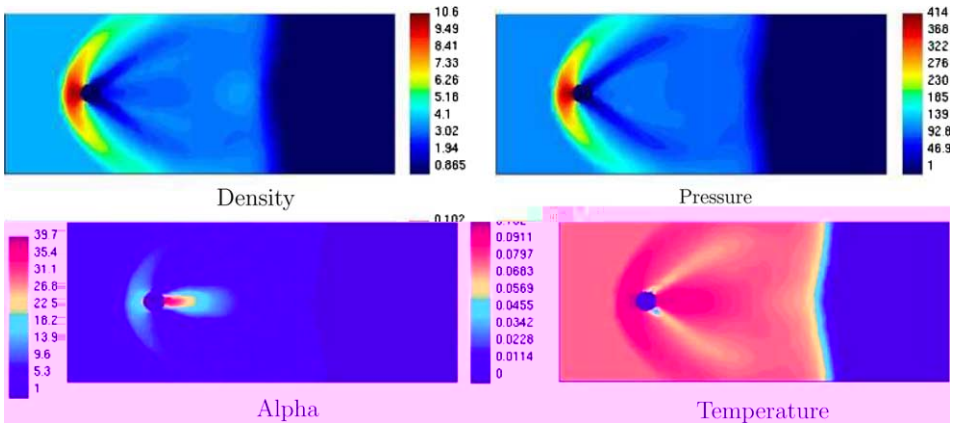


Fig. 19. Planar ionizing shock (with $\Theta = 30$) moving away the circular obstacle obtained on the mesh shown in Fig. 16.

survives the strong perturbation due to the obstacle and resumes its original planar shape and characteristics far away from the latter, thus extending the theoretical prediction of linear stability [2] observed in Section 4.4, into the nonlinear regime. In addition, it is seen that a bow shock is forming in front of the obstacle. Indeed, for high enough Mach numbers the flow behind the shock is supersonic in the laboratory frame. Furthermore, the Mach number behind the shock (defined by the flow velocity in the laboratory frame) when ionizations are taken into account is bigger than its classical gas-dynamical counterpart, due to the drop in the downstream temperature. As a result, a bow shock is indeed expected due to the steady supersonic flow over the circular obstacle. It is interesting to notice that a further increase in the density occurs behind the bow shock, i.e., between the bow shock and the circular obstacle. Whereas the initial density jump is 4.16, the density in areas adjacent to the bow shock can rise as high as 10 times the upstream density. Even more striking is the behavior of the ionization degree. The initial downstream ionization is 0.7% and one might be tempted to neglect effects of ionization all together throughout the entire flow. However, due to the rise in temperature behind the bow shock and due to the decrease of the density next to the obstacle, high ionization areas are formed with ionization degrees as high as 10% or more. This

demonstrates the importance of including the effects of ionization in calculating complex flows even when they appear initially unimportant.

## 5. Conclusion

A new wave model and numerical solution algorithm for the solutions of ionized gas (in thermal equilibrium) is presented along with its visual properties. The numerical scheme is based on evaluating mesh fluctuations for the solved variables and distributing them to the nodes of these meshes by an upwinding strategy. The numerical technique of solving the nonlinear equation of state (including electronic effects) by means of Newton type root finding algorithm is presented along with the main solution algorithm. The accuracy study and correct Euler limit (when ionization is negligible) are presented and compared to previously published results. The stability of a stationary hypersonic shock which separates non-ionized and partially ionized regions case is presented. It was shown (by a shock and obstacle interaction) that the effects of ionization in calculating complex flows should be included even when they appear initially negligible. The code is currently being modified to include the case when the heavy particles (ions and neutrals) have different temperatures than electrons.

## Acknowledgments

The memory of Prof. Igor Rutkevich and the initial contributions of him to this project will never be forgotten. Without his encouragements, this project would be impossible to be finished. In addition, the financial support by the Collaborative Research Grant programme of NATO is highly acknowledged.

## References

[1] N. Aslan, A visual fluctuation splitting scheme for magneto-hydrodynamics with a new sonic fix and Euler limit, J. Comput. Phys. 197 (2004) 1–27.
[2] M. Mond, I.M. Rutkevich, Spontaneous acoustic emission from strong ionizing shocks, J. Fluid Mech. 275 (1994) 121–146.
[3] M. Mitchner, C.H. Kruger, Partially Ionized Gases, John Wiley, New York, 1973.
[4] N. Aslan, MHD-A: a fluctuation splitting wave model for planar magnetohydrodynamics, J. Comput. Phys. 153 (1999) 437–466.
[5] M. Rudgyard, Multidimensional wave decompositions for the Euler equations, in: International Conference on Numerical methods in Fluid Dynamics, Rome, Italy, July 1992.
[6] N. Aslan, Computational investigations of ideal MHD plasmas with discontinuities, Ph.D. Thesis, University of Michigan, Nuclear Engineering Department, USA, 1993.
[7] E. van der Weide, Compressible flow simulation on unstructured grids using multidimensional upwind schemes, Ph.D. Thesis, von Karman Institute, Universite Libre de Bruxelles, 1998.
[8] M. Mond, I.M. Rutkevich, E. Toffin, Propagation and stability of strong shocks in gases, Phys. Rev. E 56 (6) (1997) 5968–5978.
[9] C.W. Shu, Total-variation-diminishing time discretizations, SIAM J. Sci. Statist. Comput. 9 (1988) 1073.
[10] A. Jameson, D. Mavriplis, Finite volume solution of the two-dimensional Euler equations on a regular triangular mesh, AIAA J. 24 (1986) 611–618.
[11] P.L. Roe, Fluctuations and signals, a framework for numerical evolution problems, in: K.W. Morton, M.J. Baines (Eds.), Numerical Methods for Fluid Dynamics II, Academic Press, New York, 1982.
[12] M. Brio, C.C. Wu, An upwind differencing scheme for the equations of ideal MHD, J. Comput. Phys. 75 (1988) 400–422.
[13] A. Zachary, P. Colella, A higher order Godunov method for the equations of ideal MHD, J. Comput. Phys. 99 (1992) 341–347.
[14] P. Londrillo, L. Del Zanna, Higher order upwind schemes for multidimensional magnetohydrodynamics, Astrophys. J. 530 (2000) 508.
[15] W.A. Wood, W.L. Kleb, On multi-dimensional unstructured mesh adaptation, AIAA Papers 99-3254, June 28, 1999.